



Originally published as:

Wuestefeld, A., Weinzierl, W. (2020): Design considerations for using Distributed Acoustic Sensing for cross-well seismics: A case study for CO₂storage. - *Geophysical Prospecting*, 68, 6, 1893-1905.

<https://doi.org/10.1111/1365-2478.12965>

Design Considerations for using DAS for Cross-Well

Seismics: A case Study for CO₂ storage

Andreas Wuestefeld¹, Wolfgang Weinzierl²

¹NORSAR

²GFZ German Research Centre for Geosciences

Andreas.Wuestefeld@NORSAR.NO

Keywords: Cross-Well Seismics, CO₂ storage, Fiber Optic

Abstract

Downhole monitoring with fibre optic DAS systems offers unprecedented spatial resolution. At the same time, costs are reduced since repeated wireline surveys can be replaced by permanent installation of comparatively cheap fibre cables. However, the single component nature of fibre data, requires novel approaches when designing a monitoring project such as cross-well seismics. At the example of the shallow CO₂ injection test site in Svelvik, Norway, we model the evolution of velocity changes during CO₂ injection based on rock-physics theory. Different cross-well seismic design scenarios are then considered to evaluate the best design and the limits of this method to detect containment breach. We present a series of evaluation tools to compare the effect of different well spacings for cross-well seismic tomography. In addition to travel-times, we also consider characteristic amplitude changes along the fibre unique to DAS strain

measurements, which might add a constrain to the inversion. We also compare the effect of using helical fibres instead of classical straight fibres. We thus present a toolbox to evaluate and compare different monitoring design options for fiber optic downhole installations for cross-well monitoring.

Introduction

Regulatory conformance verification requires detailed understanding of the pathways of the CO₂ plume during injection of CO₂ into the subsurface. Several geophysical methods can be employed to monitor the plume migration, and we here focus on cross-well seismics. We address this in a series of pre-operational leakage-scenario simulations to evaluate fibre-optic DAS responses in a cross-well seismic program. These simulations are then used to evaluate the best monitoring strategy and resolution limits of such cross-well monitoring program, which ultimately helps to measure conformance during operation.

Cross-well seismic allows for high accuracy and resolution in characterising velocity changes within the subsurface. This is particularly useful if the location of the expected change is known. The revitalization of the Svelvik CO₂ field test site (Barrio *et al.* 2014; Ringstad *et al.* 2018) bridges the gap between laboratory and commercial field scale. The field test site provides a unique opportunity to develop monitoring strategies aimed at increasing the value of information obtained from several monitoring streams. The CO₂ injection at Svelvik is into unconsolidated sands at a shallow depth of only 65 m (e.g. Eliasson *et al.* 2018; Ringstad *et al.* 2018; Weinzierl *et al.* 2018). The CO₂ is indeed not expected to remain in the injection interval on the long term. The injected gas is expected to migrate slowly out of the subsurface.

This provides a unique opportunity to test different leakage detection techniques. One of the methods employed at Svelvik is cross-well seismic, which will provide a characterisation of subsurface velocity changes with high accuracy. In addition to traditional geophones, four monitoring wells will be equipped with fibre-optic cables for DAS measurements to verify conformance.

Here we present a synthetic study to assess the sensitivity of a seismic cross-well acquisition using DAS measurements. Velocity changes due to CO₂ injection at the field test site are thus simulated. Various numerical models of the CO₂ plume evolution are realized at numerous time steps during injection. These models simulate CO₂ containment in the target zone, as well as containment breach into the cap-rock. Ultimately, comparing these simulations with recordings from real injection cases can guide conformance assessment. We evaluate how different observation well-spacings affect efficient monitoring of the evolution of the CO₂ plume. Additionally, we evaluate the benefits of helically wound fibres compared to conventional straight fibres. Different wrapping angles of the helical fibre are considered. Furthermore, we present a method to identify critical shot-receiver combinations, which should help to provide more cost-efficient time-lapse monitoring.

Modelling Velocity Changes from CO₂ Injection at Svelvik

The Svelvik ridge peninsula, located approximately 50 km SW of Oslo, Norway is classified as a glaciofluvial-glaciomarine terminal deposit. The peninsula has an extent of 1.5 km and the area-of-interest (AOI) is located in the flat, excavated part of a sand and gravel quarry. Remaining, not excavated, parts of the deposit forms small hills to the north of the study area

(Figure 1). The site is characterized by highly variable grain deposits with pebble and cobble beds in the overburden (Barrio *et al.* 2014). The bedrock depth is estimated between 300-400 m and the central part of the ridge topography reaches approximately 70 m above mean sea level. Laminated sheets of sand and silt/clay are inferred from a previous acquisition campaign (Bakk *et al.* 2012). The injection target modelled here is at 65 m depth below sea level.

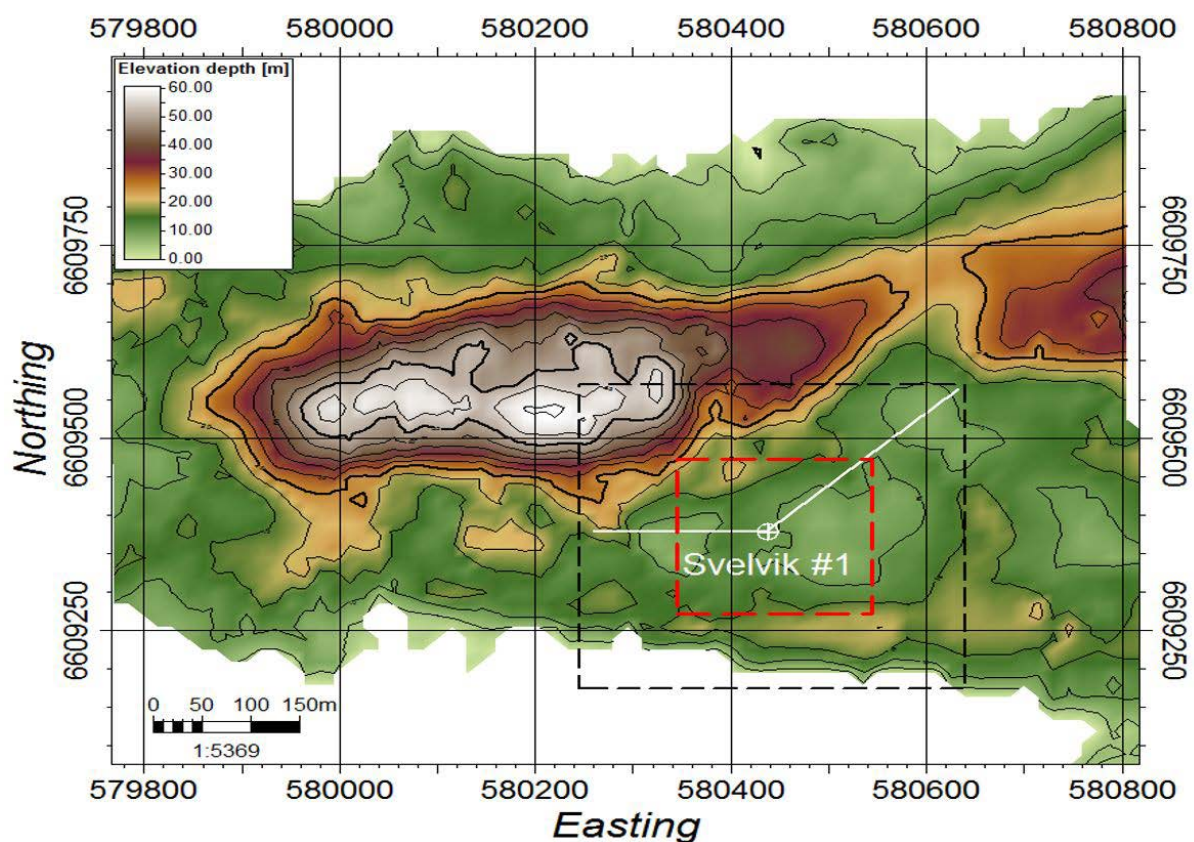


Figure 1: The Svelvik ridge topography and location map of the planned injection campaign. Well logs from the appraisal well Svelvik#1 in the centre of the white cross section were used to develop the simulation model marked by the red area-of-interest.

Figure 2 shows the clay content (V_{cl}) and grain size distribution used in determining the porosity in the centre of the cross-section from Figure 1. Clay content (V_{cl}) derived from a gamma log (GR) allows localization of an aquifer at approximately 65 m depth (Hagby 2018).

The cumulative grain size distribution at depths along the appraisal well supports this. While the geology- and core-analysis suggests a highly anisotropic and heterogeneous lamination of the sub-surface we simplify the static model by defining a cap-rock and aquifer zone. The cap-rock is confined by the zones Top Mud 1 and Top Sand 2 which also marks the boundary between the storage formation and seal (Figure 2).

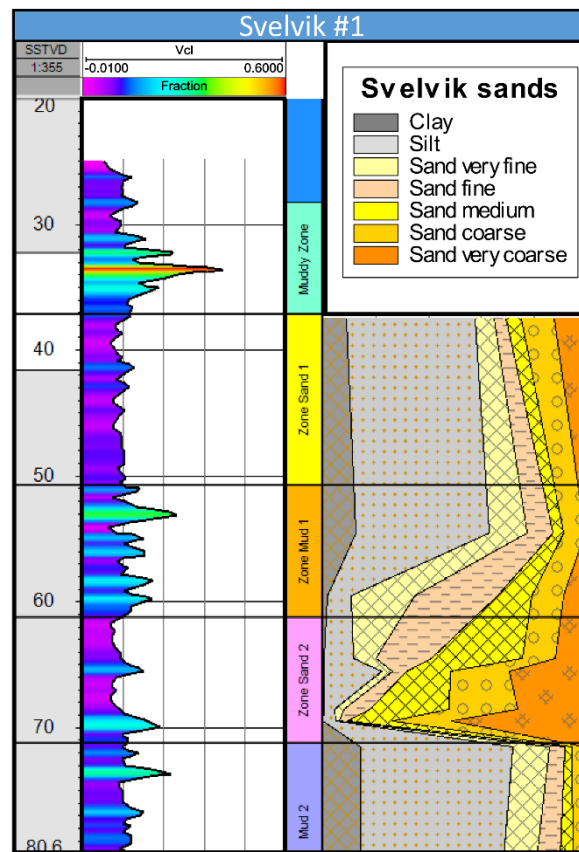


Figure 2: Selected borehole logs for the Svelvik site. V_{cl} log is displayed in the leftmost track. Followed by the zonation log is the summation track of the grain size distribution (modified after Hagby 2018)

Porosities ϕ are obtained using a sonic log for compressional velocity (V_P) via the Greenberg-Castagna relation (Equation 1; Greenberg and Castagna 1992):

$$V_P = a_C + b_C \phi + c_C V_{cl} \quad (\text{Eq. 1})$$

We chose the following parameters: $a_c = 5.81$, $b_c = -9.42$, and $c_c = -2.21$. Parameters are chosen according to the highly unconsolidated environment, similar to the geologically young Gulf Coast reservoirs like the Frio formation. A more rigorous derivation would require additional and costly appraisal well logging. While the following simulation is certainly affected by the inconclusive derivation of the underlying regression coefficients the sensitivities obtained by the scenario-based approach are indicative for a targeted active survey.

Furthermore, from these porosities we derive permeabilities κ using the Kozeny-Carman rule (Equation 2) with averaged mineral sphere diameters $d = 0.0035 \text{ mm}$ obtained from the coarse- to fine grain-size distributions (Figure 2). The tortuosity ($\tau \sim 0.25$) dependent factor $B = 0.23$ (Carman 1961) is chosen based on hydraulic conductivity tests showing a permeability of roughly 150 mD. No anisotropy for the hydraulic conductivity is set, i.e. $\kappa_z/\kappa_h=1$. While a rigorous derivation of permeabilities would include a grain size as well as V_{cl} dependent definition, for the purpose of this DAS design study we rather keep the parameters constant over the entire static model.

$$\kappa = \frac{1}{72 \tau^2} \frac{\phi^3}{(1-\phi)^2} d^2 = B \frac{\phi^3}{(1-\phi)^2} d^2 \quad (\text{Eq. 2})$$

Three different CO₂ containment cases are considered here: high-, base-, and low-containment. Porosities and permeabilities, which are directly linked to the sonic log, are at this point considered the base-scenario. Low- and high-cases are derived with a percentage increase and decrease of the porosities and permeabilities in the seal and storage formation. The multiplication factors within the seal and storage formation are listed in Table 1.

The corresponding high, base and low values are chosen to minimize (low) and maximize (high) the saturation footprint accordingly. Therefore, a higher permeability in the seal with a lower permeability in the aquifer should ultimately favour a leakage scenario, where the extent of the CO₂ plume would be limited as a result of increased seal penetration.

For all three scenarios individual capillary entry pressures for the cap-rock are defined using a Brooks-Corey model (Brooks and Corey 1966). The capillary pressure, P_c , is defined by

$$P_{c,g} = P_{e,g} \left(\frac{S_g - S_{g,r}}{1 - S_{g,r}} \right)^{-1/\lambda}, \quad (\text{Eq. 3})$$

where *subscript g* refers to CO₂. $P_{e,g}$ is then the minimum required displacement pressure for CO₂ entering a brine-saturated rock, S_g the CO₂ saturation, and $S_{g,r}$ the irreducible CO₂ saturation. With the pore size dependent parameter λ , parameters $(\lambda, S_{g,r}) = (3, 0.1)$ are kept constant. This additional assumption aims at containing the injected CO₂ for the high case and allowing for an increased seal penetration for the low scenario. The values for the individual entry pressures for the simulation scenarios are listed in Table 2.

[Table 2 approximately here]

We are using Eclipse 300 for the simulation of CO₂ migration and pressure build-up due to injection. The static structural model is based on interpretation performed during a previous site characterization campaign for which two 2D seismic reflection profiles were acquired (Barrio *et al.* 2014). After well log upscaling of the porosities and permeabilities they are populated laterally constant in each layer for the individual simulation scenarios. As the formation targeted during the injection is very shallow the injected CO₂ is in a gaseous state, and migration is mapped with a constant injection rate of 200 Sm³/day (approximately 16

kg/h) (Grimstad *et al.* 2018). The comparatively low injection rates are chosen to minimize any irreversible subsurface alteration of the test set. The boundary conditions are set to no-flow resulting in a comparatively high pressure-increase. While pressure changes generally affect the seismic velocities, this effect is at least an order of magnitude lower than that of the increasing saturations and no further constraints are imposed on the simulations. Figure 3 shows the resulting CO₂ saturation (S_g) footprint of the simulation cases after the injection of approximately 12600 m³ (23 t) CO₂. Seal leakage is clearly observed for the low-case, and saturations in the overburden decrease as the seals capillary entry pressures for the CO₂ increase for the base- and high-case.

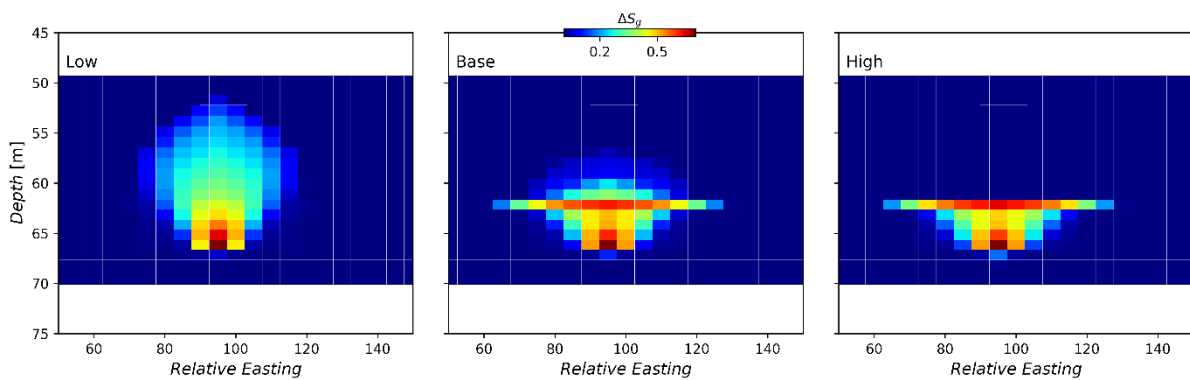


Figure 3: Cross section through the injection location showing the saturation footprint of the High/Base/Low simulation cases after injecting approximately 23 tons of CO₂.

To assess the elastic parameters required for raytracing we perform a conventional fluid substitution using the equation from Gassmann (Gassman 1951; Avseth, Mukerji and Mavko 2010). The Frame material consist of Sand and Clay with fractions of each defined by V_{cl} and $(1-V_{cl})$. Upper and Lower Hashin-Shtrikman bounds are computed and subsequently mixed based on a solid mixing factor S_m (Hashin and Shtrikman 1963). On acquisition of the baseline before injection the subsurface is fully brine saturated, which is replaced by CO₂ during injection. Fluid moduli and densities of brine and CO₂ are mixed based on a Voigt-

Reuss average with a fluid mixing factor F_m . The pressure dependence of the dry rock frame is incorporated by an effective pressure dependence equation outlined in Avseth *et al.* (2010). Using the clay content V_{cl} , bulk and shear moduli (K , G) and effective density (ρ) of the saturated rock frame material as well as the individual mixing ratios (S_m , F_m) for the solid and fluid phase, respectively, it is possible to compute V_p , V_s and mean density ρ , at each grid cell for each time step. To assess the uncertainties inherent in the acquisition system we define prior uncertainties on the rock physics parameters described above. Assuming stochastic independence between these rock physics parameters, and performing 100 model realizations based on normal distributions with the mean and standard deviation shown in Table 3, it is possible to assess probable uncertainties on the acquisition in a DAS survey. [Table 3 approximately here]

DAS modelling

Cross-well seismic is typically used for velocity tomography. Such tomographic methods employ travel-time differences between all shot-receiver combinations to invert for the velocity structure. Repeat surveys can identify and locate changes in the velocity structure. This implies accurate travel-time picks, which in turn requires a sufficiently high signal-to-noise ratio (SNR). Note that in fibre-optic DAS systems, the amplitude of the signal not only depends on attenuating effects and geometrical spreading, but also on the incidence angle θ of the wave relative to the fibre (e.g. Kuvshinov 2016). Assuming a spherical radiation pattern of the source, this dependence on incidence angle is the dominant effect for amplitude observed changes. This so called “broadside sensitivity” is due to the effect that waves perpendicular to the fibre do not generate strain on that fibre. For P-waves, the amplitude decays are proportional to $\cos^2\theta$, while for S-waves the amplitude follows a $\sin 2\theta$ function

(e.g., Kuvshinov 2016; Wuestefeld and Wilks 2019). Assuming perfect coupling between the fibre, cable, and the surrounding rock mass, Kuvshinov (2016) derived equations for strain amplitude gain (or loss) due to helically wound fibres with a wrapping angle α . For P-waves the equation is given as (Kuvshinov 2016):

$$\Gamma_P = \cos^2\theta \sin^2\alpha + \frac{(\lambda_R + 2\mu_R) - (\lambda_c + 2\mu_R)\cos^2\theta}{2(\lambda_c + \mu_c + \mu_R)} \cos^2\alpha, \quad (\text{Eq. 4})$$

where μ and λ are the Shear Modulus and 1st Lamé constant, respectively, and the subscripts “c” and “R” indicate the elastic parameter for the cable and the rock mass. Note how in the case of a straight fibre ($\alpha = 90^\circ$) this equation reduces to $\Gamma_P = \cos^2\theta$.

Thus, for vertical wells, P-waves traversing the CO₂ plume horizontally are most affected by the velocity changes, but travel-times cannot be picked due to low amplitudes.

We simulate the cross-well study by placing several shots and DAS sensing positions along simulated monitoring- and shot-wells. We only here consider the low- and high-containment cases, between which we expect the largest difference. The well position relative to the injection is then altered to simulate different well spacings. Figure 4 shows this for well spacings of 20m and 40 m, respectively. The background reflects the velocity model, for two cases: before injection (Day 0), and at the end of injection (Day 63) for the high- and low-containment cases.

While the choice of parametrization for the V_P -pressure-dependence is rather arbitrary we choose to imply a decrease of V_P for increasing pressure. The rock matrix is assumed to react with an opening of cracks for increasing pressures. A more rigorous formulation would require to simulate the fracturing as a pressure dependent porosity increase. Following the

parametrization in Avseth *et al.* (2010) the pressure increase is softening the rock frame with an effective change between any two effective pressures. This can be seen in the somewhat slower velocities, not only near the plume (Figure 4). Ray paths for first arrivals at all receivers of a shot at 80m depth are also plotted. These are determined using an Eikonal solver. The plume causes the rays to bend and thus arriving at the sensors at different times and incidence angles, compared to both, the initial Day 0 simulation and the different post-injection containment scenarios. These differences are shown in Figure 5.

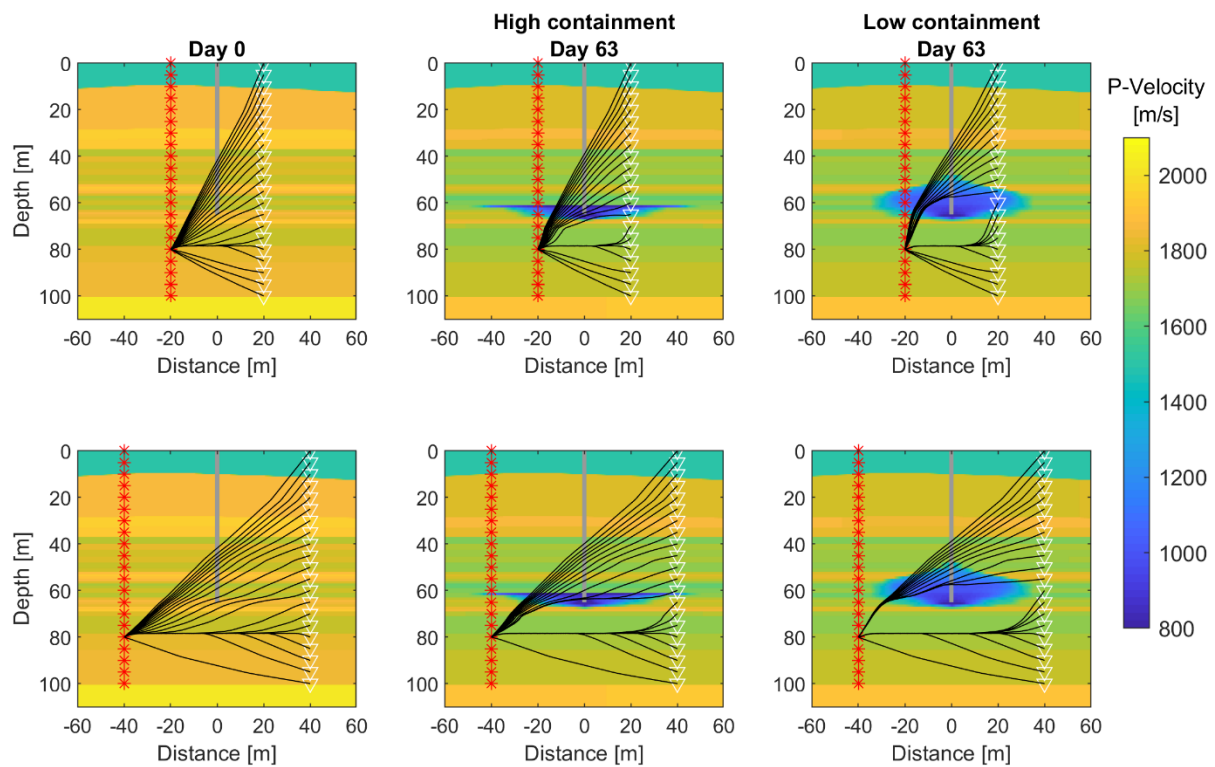


Figure 4: Velocity models and ray paths for a shot at 80 m depth for different containment scenarios. We show two potential well spacing 20 m (top row) and 40 m (bottom row).

Changes in ray paths not only affect travel-times, but also the incidence angles (and thus recorded amplitude) on the recording fibre. Figure 5 shows maps of travel-time differences between pre-and post-injection for all shot-receiver combinations at 20 m well spacing (as shown in Figure 4, top row). All panels are organized such that the receiver depths are the

214 rows and shot depths the columns. Thus, each “pixel” represents a certain shot-receiver
215 combination. For travel-times, these maps are symmetric, reflecting reciprocity of shot and
216 receiver. In contrast, incidence angle maps are asymmetric, since take-off and incidence
217 angles are different for any combination. Ray paths between combinations of both shallow
218 shots and shallow receivers are not affected by the developing plume. This is also true for the
219 deepest shot-receiver combinations.

220 The high-containment case (Figure 5a) shows sharp edges in travel-times below the injection
221 depth. In the low-containment case (Figure 5b), the edges are smoother, and, most notably,
222 the travel-time difference to the pre-injection is much stronger (up to about twice). Figure 5c
223 shows travel-time difference between the low- and high containment cases, at the end of
224 injection. Thus, it indicates which shot-receiver combinations are relevant for distinguishing
225 between either case.

226 The bottom row of Figure 5 (d-f) shows the incidence angle differences. The high-containment
227 case shows that relatively few shot-receiver combinations are affected. In the low-
228 containment case (Figure 5e), the rays are bend more during the injection. Also note the
229 polarity flip in incidence angle below 40 m depth. Differences between low- and high-
230 containment can be manifested in incidence angles (Figure 5f), since changes in incidence
231 angle result in characteristic changes in recorded amplitudes at the fibre (Figure 6).

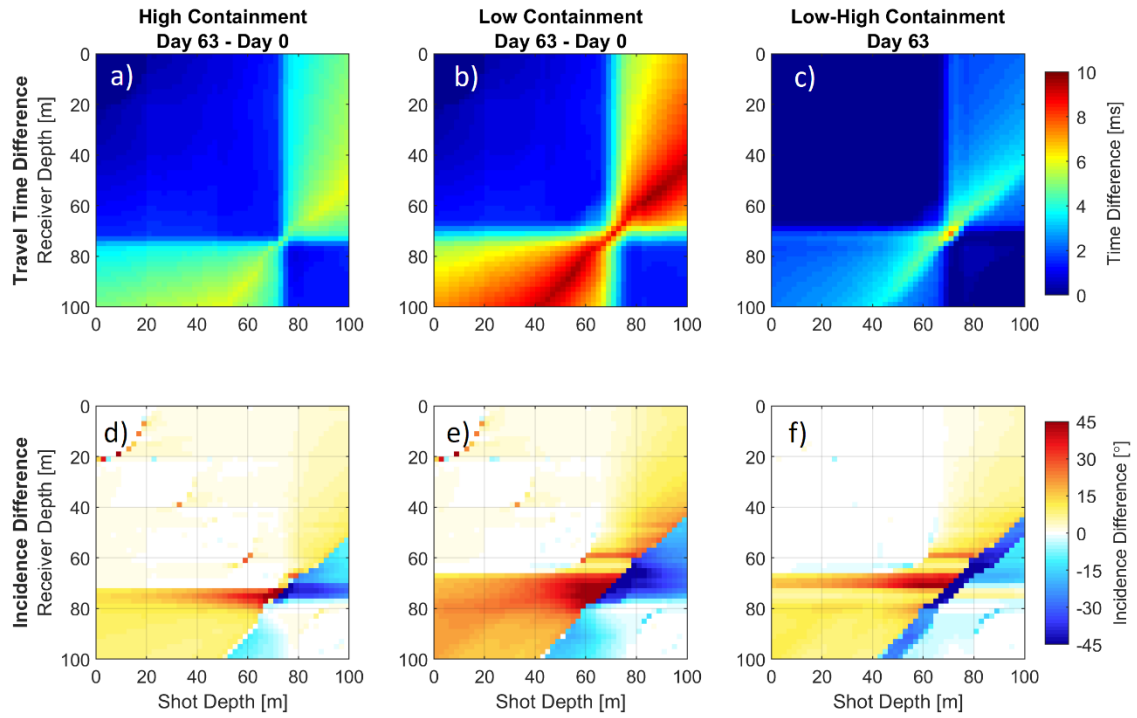


Figure 5: Travel time (a-c) and incidence angle differences (d-f) of all shot-receiver combinations. Each panel shows the parameter change for all combinations of shot and receiver depth. Note that travel time panels are symmetric due to shot/receiver reciprocity, while incidence angle panels are asymmetric.

The changes in travel-times in Figure 5 reflect the changes in velocity model between pre- and post-injection. Both ray-lengths and travel-times are affected by changes of the velocity model. Moreover, amplitudes are also affected by different ray length due to geometrical spreading and attenuation. For a better understanding of these changes, Figure 6 shows the temporal evolution in 7-day intervals, both for ray-path length and travel-times. We compare at each interval the high- and low-case at 20 m well spacing.

For the high-containment scenario a decrease in ray-length corresponds to smaller travel-time changes relative to the surrounding paths. The plume stabilises early (~21 days) as shown by only minimal changes in either path length or travel times at later stages. For the low-

containment case the areas of increased ray-length continue to later stages and coincide with similar increases in travel-time. The largest change occurs in the first week of injection, with up to 3.8 m longer ray paths (equal to 8.5% elongation). However, most elongation is below 2 m. The significance of these changes must be evaluated in the design stage of any project individually, and compared to expected changes of Fiber Illumination resulting from the broadside sensitivity. Approximating the media as homogeneous the geometrical spreading factor is calculated as $1/r$, with r being the ray length. Then, in the case presented in Figure 6, geometrical spreading differences ($1/r_{t=2} - 1/r_{t=1}$) are at maximum 0.002 for any given time interval. This effect can thus be neglected here compared to the Fiber Illumination factors. Note that additional amplitude dependency may be introduced from the source radiation pattern, which is here assumed to be perfectly spherical. Repeatability of the source might also be affected by changes in coupling and frequency content. We furthermore assume that the gauge length has been chosen optimally, for example by following the approach by Dean, Papp and Hartog (2015), and Dean, Cuny and Hartog (2017)

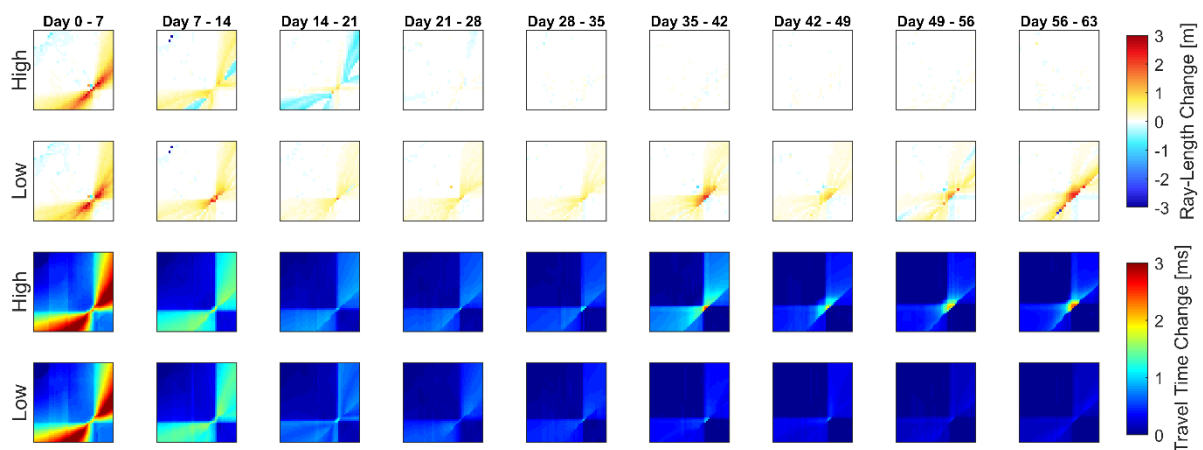


Figure 6: Evolution of changes in ray-length (top two rows) and travel-time (bottom two rows). Each panel shows the change relative to the previous week of injection for high- and low-containment case.

Before discussing the simulated effects of the amplitudes in more detail, we first look at the travel-times. Changes in our model cause travel-time changes, and the question is if these changes are large enough to be detected. Assuming a pick accuracy of 2 samples, and a sampling rate of 4000 Hz, that means that only changes above 0.5 ms can be resolved confidently. Thus, we apply a threshold filter to the travel-time maps: Only shot-receiver combinations above that threshold are significant. Figure 7 shows such significance maps. We here choose to show as an example only changes during one week of injection (Day 14 – Day 21). As discussed earlier, for each containment scenario, we generated 100 realisations, to allow for a statistic variation of the rock-physics parameters (see Table 3). These variations are included in the significance maps of Figure 7: In the top row, black areas identify shot-receiver combinations not showing any changes above the threshold for any of the realisations. White areas are always above that threshold. Grey indicates that these combinations are significantly affected for some realisations. The high-containment case results in sharp contrasts at shot and receiver depths of 70 m. In the low-containment case, the contrast is blurred, indicating the spread in plume extent between the multiple realisations.

This spread also highlights that this method can be applied within repeat-surveys to monitor the plume and detect conformance issues. To help identifying such issues we propose to not only compare the maps, but calculate the sum of significant receivers per shot. Such an approach also helps to identify which shots and receivers contribute to the determination of conformance issues, which helps in planning and design phase to manage costs. The bottom row of Figure 7 shows these distributions of “shot significance”: The black line is the median

287 over all realisations of the sum of receivers above threshold for each shot depth. The grey
288 area represents the 2σ confidence interval.

289 Evidently, the different ray paths (Figure 4) in the high- and low-containment models result
290 in characteristically different “shot significance” curves (Figure 7, bottom row). Perhaps
291 interestingly, while the high-containment case shows sharper contrasts in depths than the
292 low-containment case: In the high-containment case the significance curve (Figure 7d)
293 gradually decreases with shot depth before increasing after 65 m shot depths. In contrast, the
294 low containment case (Figure 7e) shows a stable number of receivers above the significant
295 travel-time changes, with a sharp drop near the injection depth of 65 m, followed by a sharp
296 increase and stable again afterwards at a high receiver count.

297 The last column of Figure 7 shows the difference between low- and high-containment cases
298 on Day 21 of the injection. Such analysis indicates how well the different scenarios could be
299 distinguished. The significance curve indicates that only shot depths between 30 and 60 m
300 and below 85 m show travel-time differences above the threshold. Only those shot depths
301 thus contribute to any potential decision on conformance.

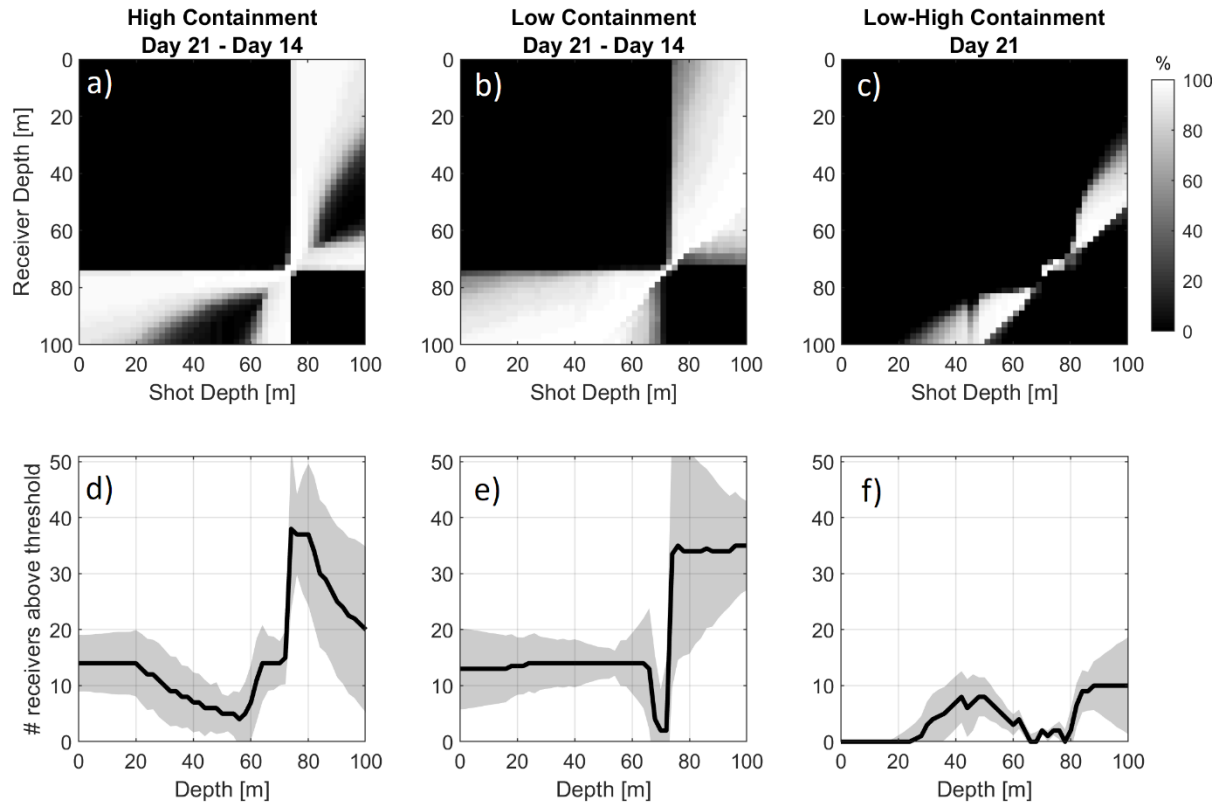


Figure 7: Significance of changes in travel times. In contrast to Figure 5a-c, only the change during 1 week of injection (Day 14 - 21) are considered. 100 realisations of each scenario (high- and low containment) is calculated. A threshold of 0.5 ms is chosen. Shot-receiver combinations below this threshold are masked. TOP: The sum of all combinations above the threshold from the 100 realisations, i.e. white means all realisations result in travel time changes above the threshold at that shot-receiver combination. Black means no realisation has changes above that threshold. BOTTOM: Median of sums for the 100 model realisations along the columns of the top row, i.e. sum of receivers for each shot depth above threshold. The 2σ confidence interval is also shown.

The previous discussion was mostly concerned with travel-time differences in the cross-well seismics. DAS records however exhibit amplitudes as an additional, characteristic parameter. In contrast to travel-times, fibre amplitudes are not reciprocal, and thus the shot-receiver maps for amplitudes (Figure 5 bottom row; Figure 8) are asymmetric. This asymmetry provides further constraints to an inversion compared to travel-times.

319 Wuestefeld and Wilks (2019) introduced the “Fibre Illumination Factor” Γ . It represents the
320 scaling of the recorded strain amplitude as a result of the broad-side insensitivity of the fibre
321 (e.g. Hornman *et al.* 2013; Ning and Sava 2016). In addition, helical fibres (e.g. Hornman *et al.*
322 2013) have been proposed to minimize the effect of this so-called broad-side sensitivity.
323 Different wrapping angles α of the helix are modelled. Figure 8 shows that a wrapping angle
324 of $\alpha=45^\circ$ shows smallest variation in Γ , and thus recorded amplitudes (assuming all other
325 parameters constant). On the one hand side this may be beneficial to assure constant picking
326 accuracy, especially in low signal-to-noise ratio environments. On the other hand, this
327 variation in amplitude scaling can be used to add constraints to an inversion algorithm (e.g.
328 Peterson, Paulsson and McEvilly 1985), thus yielding more robust interpretations.

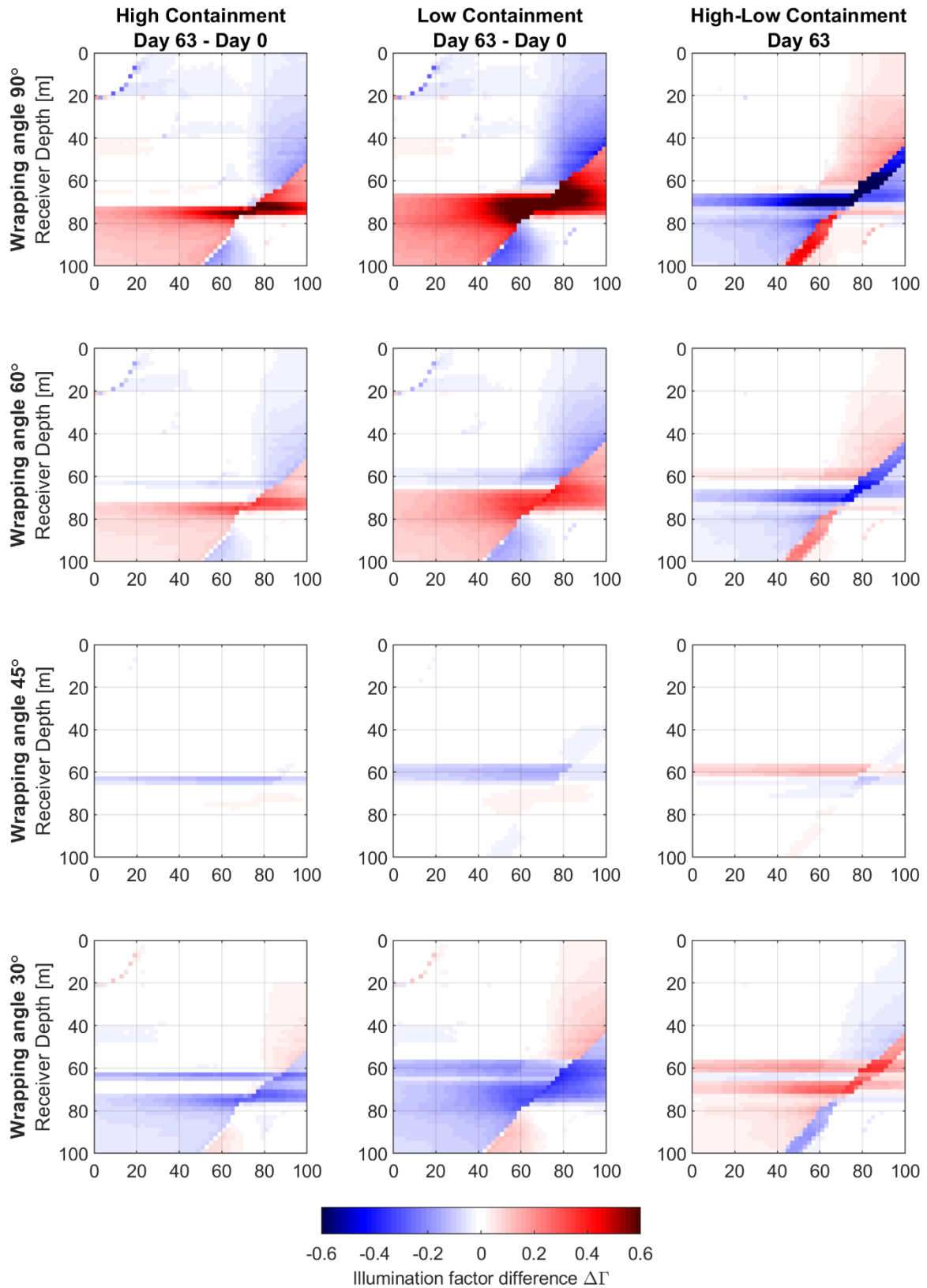


Figure 8: Differences in Fibre Illumination (scaling) factor. Each row represents a different wrapping angle of helical fibre (90° is a conventional, straight fibre).

Similar to the (static) travel-time significance curves between pre- and post-injection (Figure 7, bottom row), we can also evaluate the temporal evolution of these significance curves. Figure 9 thus shows the temporal evolution of “significance”, i.e. percentage of shots above a threshold, for Fibre Illumination differences, $\Delta\Gamma$. We choose a threshold of 0.1Γ (i.e. 10% amplitude change). Furthermore, the differences are calculated in 4-week long sliding windows. Note that these amplitude changes only reflect the effect of incidence angle on the fiber. When inverting real data for velocity changes, these need to be corrected for before ray paths effects can be inverted for.

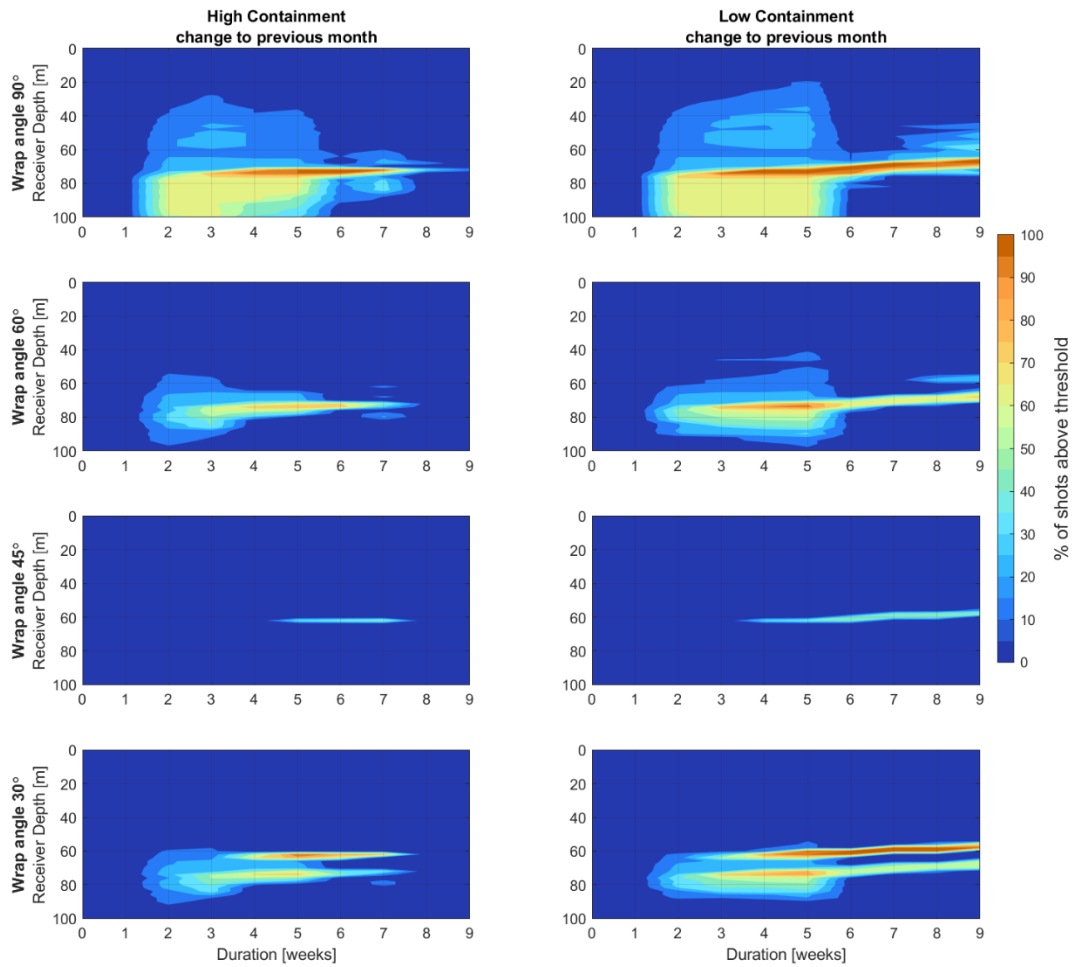


Figure 9: Evolution of $\Delta\Gamma$ for different wrapping angles, in the high (left column) and low (right column) containment case. We use a 4-week sliding window, and a threshold of $\Gamma=0.1$

Containment to the target zones is one of the main concerns of CO₂ storage projects. Leakage into the overburden should be detected with a given monitoring method. It is therefore crucial to determine the capabilities of the method in the planning phase and find the best design beforehand. For cross-well seismic the variable design parameters are well spacing, repeat frequency, and relevant shot-receiver depths. In addition, systems using DAS records need to consider the wrapping angle of the fibre. Figure 10 thus shows the evolution of the differences in both travel-times and Fibre Illumination $\Delta\Gamma$ for different well spacings. Differences are calculated in a 4-week window. Thresholds are identical to Figures 7 and 9, i.e. 0.5 ms and 0.1 Γ , respectively.

Differences in travel-times between low- and high-containment cases can be seen already two weeks after the injection start (see also Figure 6), i.e. conformance issues can be detected already two weeks after injection start. Shorter well spacings result in more pronounced effects. During injection the number of receivers above the selected threshold increase and moves towards more shallow receivers depths (as indicated by the orange “wedge” in Figure 10, top row). This effect gets less pronounced for larger well spacings. Fibre Illumination also shows a wedge-like evolution, and for all wrapping angles, albeit these changes are significant only after four to five weeks. Again, a wrapping angle of 45° shows only very little change in Γ (see also Figure 8). Some combinations of wrapping angle and well spacing result in very pronounced double wedges, below and above the injection depth (65 m), respectively. This could also be seen in Figure 9. At 20 m well spacing even a third wedge is visible near 80 m depth for helical cables. Such features will be valuable in interpreting real data for cap-rock integrity.

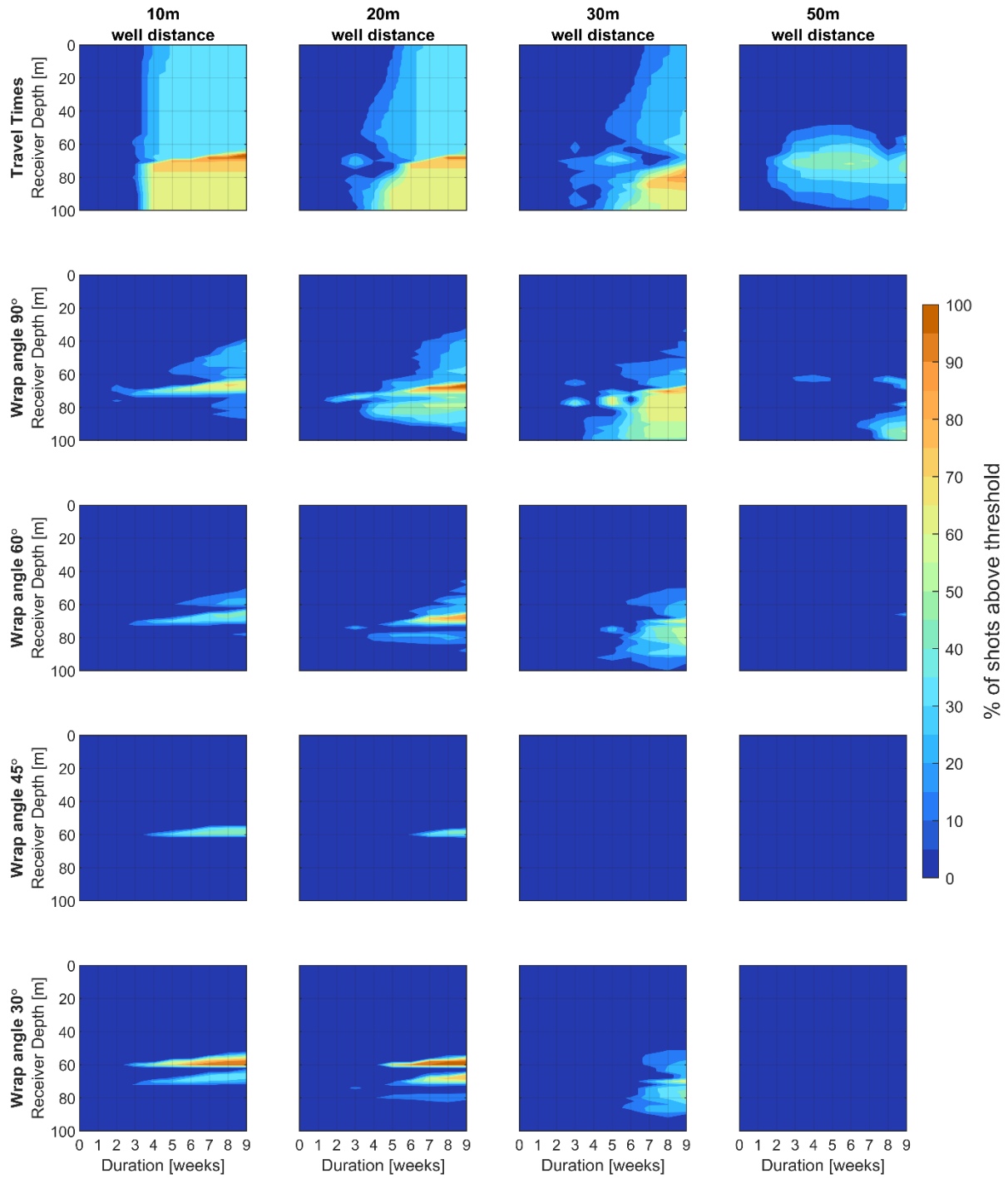


Figure 10: Evolution of the difference between low- and high-containment case, for travel time (top row) and $\Delta\Gamma$ (row 2 to 4). Different wrapping angles and different well spacings are considered.

371 **Conclusion**

372 For an upcoming injection campaign several CO₂ migration scenarios have been defined.
373 Within a rock physical context, the simulation results are translated into elastic parameters
374 and raytracing in a cross-well configuration performed. The dynamic simulation models are
375 parametrized such that leakage into the overburden is favoured, plausible, or completely
376 inhibited.

377 Ray tracing is used to obtain an ideal configuration for the monitoring well positions and
378 wrapping angles for the helical fibres. With increasing volumes of injected CO₂ the observed
379 travel-time as well as illumination factor differences are used to distinguish the simulation
380 scenarios. Sources, illuminating the zone of interest, are identified based on their resolution
381 power. This will aid in history matching and updating the dynamic model parametrization.
382 The value of information a specific shot yields helps to focus the acquisition campaigns during
383 the injection phase as only one source will be available.

384 We showed that shorter well spacings (10 and 20 m in the Svelvik case) are better suited to
385 identify changes in the subsurface with the cross-well seismic technique. Helical fibres provide
386 some advantages, for example a wrapping angle of 45° muted nearly all amplitude variations.
387 This allows for consistent picking. On the other hand, straight fibres may be better suited if
388 the effect of amplitude variation can be included to constrain the inversion.

389 The simulation and forward modelling of anticipated elastic responses not only provided an
390 input to an idealized acquisition setup but also outlined approaches to conformance
391 verification. The risk of leakage is driven by plume migration and as such by a conceptual
392 understanding of reservoir heterogeneities. Pre-operational considerations are required to

393 develop cost-efficient approaches in measurement, monitoring and verification of CO₂ plume
394 migrations.

395

396 **Acknowledgments**

397 We want to thank the Associate Editor and two anonymous reviewers for their comments and suggestions,
398 which helped to improve this manuscript. Furthermore, we want to thank the ECCSEL Svelvik CO₂ Field Lab for
399 access to reports and data.

400 This publication has been produced with support from the Pre-ACT project (Project No. 271496) funded by
401 RCN (Norway), Gassnova (Norway), BEIS (UK), RVO (Netherlands), and BMWi (Germany) and co-funded by the
402 European Commission under the Horizon 2020 programme, ACT Grant Agreement No 691712. We also
403 acknowledge the industry partners for their contributions: Total, Equinor, Shell, TAQA

404

405 **Figure Captions**

406 Figure 1: The Svelvik ridge topography and location map of the planned injection campaign.
407 Well logs from the appraisal well Svelvik#1 in the centre of the white cross section were used
408 to develop the simulation model marked by the red area-of-interest.

409 Figure 2: Selected borehole logs for the Svelvik site. Vcl log is displayed in the leftmost track.
410 Followed by the zonaton log is the summation track of the grain size distribution (modified
411 after Hagby 2018).

412 Figure 3: Cross section through the injection location showing the saturation footprint of the
413 High/Base/Low simulation cases after injecting approximately 23 tons of CO₂.

414 Figure 4: Velocity models and ray paths for a shot at 80 m depth for different containment
415 scenarios. We show two potential well spacing 20 m (top row) and 40 m (bottom row).

416 Figure 5: Travel time (a-c) and incidence angle differences (d-f) of all shot-receiver
417 combinations. Each panel shows the parameter change for all combinations of shot and
418 receiver depth. Note that travel time panels are symmetric due to shot/receiver reciprocity,
419 while incidence angle panels are asymmetric.

420 Figure 6: Evolution of changes in ray-length (top two rows) and travel-time (bottom two
421 rows). Each panel shows the change relative to the previous week of injection for high- and
422 low-containment case.

423 Figure 7: Significance of changes in travel times. In contrast to Figure 5a-c, only the change
424 during 1 week of injection (Day 14 - 21) are considered. 100 realisations of each scenario
425 (high- and low containment) is calculated. A threshold of 0.5 ms is chosen. Shot-receiver
426 combinations below this threshold are masked. TOP: The sum of all combinations above the
427 threshold from the 100 realisations, i.e. white means all realisations result in travel time
428 changes above the threshold at that shot-receiver combination. Black means no realisation
429 has changes above that threshold. BOTTOM: Median of sums for the 100 model realisations
430 along the columns of the top row, i.e. sum of receivers for each shot depth above threshold.
431 The 2 σ confidence interval is also shown.

432 Figure 8: Differences in Fibre Illumination (scaling) factor. Each row represents a different
433 wrapping angle of helical fibre (90° is a conventional, straight fibre).

434 Figure 9: Evolution of $\Delta\Gamma$ for different wrapping angles, in the high (left column) and low (right
435 column) containment case. We use a 4-week sliding window, and a threshold of $\Gamma=0.1$.

436 Figure 10: Evolution of the difference between low- and high-containment case, for travel
437 time (top row) and $\Delta\Gamma$ (row 2 to 5). Different wrapping angles and different well spacings are
438 considered.

439

440 **References**

- 441 Avseth P., Mukerji T. and Mavko G. 2010. Quantitative seismic interpretation: Applying rock
442 physics tools to reduce interpretation risk. *Cambridge University Press*.
- 443 Barrio M., Bakk A., Grimstad A.-A., Querendez E., Jones D. G., Kuras O., Gal F., Girard J.-F.,
444 Pezard P., Depraz L., Baudin E., Børresen M. H. and Sønneland L. 2014. CO₂ migration
445 monitoring methodology in the shallow subsurface: Lessons learned from the CO₂
446 FIELDLAB project. *Energy Procedia* 51, 65-74
- 447 Bakk A., Girard J. F., Lindeberg E., Aker E., Wertz F., Buddensiek M., Barrio M. and Jones D.
448 2012. CO₂ field lab at Svelvik ridge: site suitability. *Energy Procedia* 23, 306-312.
- 449 Brooks R. H. and Corey A. T. 1966. Properties of porous media affecting fluid flow. *Journal of*
450 *the Irrigation and Drainage Division* 92(2), 61-90.
- 451 Carman P. C. 1961. L'écoulement des gaz a travers les milieux poreux. Institut National des
452 Sciences et Techniques Nucleaires. Saclay (in French)
- 453 Dean T., Papp B. and Hartog A. 2015. Wavenumber Response of Data Recorded Using
454 Distributed Fibre-optic Systems. 3rd EAGE Workshop on Borehole Geophysics, Athens,
455 Greece, Extended Abstracts, BGP07.
- 456 Dean T., Cuny T. and Hartog A.H. 2017. The effect of gauge length on axially incident P-waves
457 measured using fibre optic distributed vibration sensing. *Geophysical Prospecting* 65(1),
458 184-193
- 459 Eliasson P., Ringstad C., Grimstad A.-A., Jordan M. and Romdhane A. 2018. Svelvik CO₂ Field
460 Lab: Upgrade And Experimental Campaign. Fifth EAGE CO₂ Geological Storage
461 Workshop, Utrecht, The Netherlands, Extended Abstracts, Th CO₂ 02.
- 462 Gassmann F. 1951. Über die Elastizität poröser Medien. *Vierteljahrsschrift der*
463 *Naturforschenden Gesellschaft* 96, 1-23.

464 Greenberg M. and Castagna J. 1992. Shear-wave velocity estimation in porous rocks:
465 Theoretical formulation, preliminary verification and applications 1. *Geophysical*
466 *Prospecting* 40, 195-209.

467 Grimstad A.-A., Sundal A., Hagby K. F. and Ringstad C. 2018. Modelling Medium-Depth CO₂
468 Injection at the Svelvik CO₂ Field Laboratory in Norway. Proceedings of 14th
469 Greenhouse Gas Technologies Conference, Melbourne, Australia.

470 Hagby K. F. 2018. Modelling Medium-Depth CO₂ Injection at the Svelvik CO₂ Field Laboratory
471 in Norway. *Master thesis, NTNU*.

472 Hashin Z. and Shtrikman S. 1963. A variational approach to the theory of the elastic behaviour
473 of multiphase materials. *Journal of the Mechanics and Physics of Solids* 11(2), 127-140.

474 Hornman K., Kuvshinov B. N., Zwartjes P. and Franzen A. 2013. Field Trial of a Broadside-
475 sensitive Distributed Acoustic Sensing Cable for Surface Seismic. 75th EAGE Annual
476 Meeting, London, UK, Expanded Abstracts, Tu 04 08

477 Kuvshinov B. N. 2016. Interaction of helically wound fibre-optic cables with plane seismic
478 waves. *Geophysical Prospecting* 64(3), 671-688

479 Ning I. L. C. and Sava P. 2016. Multicomponent distributed acoustic sensing. 86th SEG Annual
480 Meeting, Dallas, Texas, USA, Expanded Abstracts, 5597-5602.

481 Mavko G., Mukerji T. and Dvorkin J. 2009. The rock physics handbook: Tools for seismic
482 analysis of porous media. *Cambridge University Press*

483 Peterson J.E., Paulsson B.N.P. and McEvilly T.V. 1985. Applications of algebraic
484 reconstruction techniques to crosshole seismic data. *Geophysics* 50(10), 1566-
485 1580

486 Ringstad C., Eliasson P., Jordan M. and Grimstad A.-A. 2018. Re-Vitalization and Upgrade of
487 the Svelvik CO₂ Field Laboratory in Norway. Proceedings of 14th Greenhouse Gas
488 Technologies Conference, Melbourne, Australia.

- 489 Weinzierl W., Wiese B., Jordan M., Schmidt-Hattenberger C., Eliasson P., Ringstad C., Lueth
490 S. and Grimstad A. 2018. Pre-operational considerations in a poro-elastic site
491 assessment for the Svelvik Field Lab. *Fifth CO2 Geological Storage, EAGE, Utrecht,*
492 *Netherlands, Expanded Abstracts, Fr CO2 P04.*
- 493 Wuestefeld A. and Wilks M. 2019. How to twist and turn a fiber: Performance modeling for
494 optimal DAS acquisitions. *The Leading Edge* 38(3), 226-231